Computers and Structures 146 (2015) 91–104

Contents lists available at ScienceDirect

Computers and Structures

journal homepage: www.elsevier.com/locate/compstruc

The MITC3+ shell element in geometric nonlinear analysis

Hyeong-Min Jeon [a], Youngyu Lee [a], Phill-Seung Lee [a,*], Klaus-Jürgen Bathe [b]

[a] Division of Ocean Systems Engineering, Korea Advanced Institute of Science and Technology, 291 Daehak-ro, Yuseong-gu, Daejeon 305-701, Republic of Korea
[b] Department of Mechanical Engineering, Massachusetts Institute of Technology, Cambridge, MA 02139, USA

ARTICLE INFO

Article history:
Received 17 June 2014
Accepted 15 September 2014

Keywords:
Shell element
3-node triangular element
Mixed finite element method
MITC method
Geometric nonlinear analysis
Large displacements and rotations

ABSTRACT

In this paper, we present the MITC3+ shell finite element for geometric nonlinear analysis and demonstrate its performance. The MITC3+ shell element, recently proposed for linear analysis [1], represents a further development of the MITC3 shell element. The total Lagrangian formulation is employed allowing for large displacements and large rotations. Considering several analysis problems, the nonlinear solutions using the MITC3+ shell element are compared with those obtained using the MITC3 and MITC4 shell elements. We conclude that the MITC3+ shell element shows, in the problems considered, the same excellent performance in geometric nonlinear analysis as already observed in linear analysis.

1. Introduction

Due to significant efforts over the past decades, the finite element method has become a powerful tool for the linear and nonlinear analyses of shell structures [2]. The available capabilities have been continuously improved in reliability and effectiveness but there are still important research and development tasks to be accomplished. One such task is the development of an optimal 3-node shell element.

When modeling complex shell structures, an effective mesh of triangular shell elements is relatively easy to generate provided general element shapes are allowed, that is, the element employed must be effective even when used in general triangular shapes. Lee et al. proposed recently the 3-node MITC3+ shell element for linear analysis that was shown to perform even well when highly distorted elements are used [1]. Hence this element is a good candidate for use in general meshes. Of course, a shell surface can also be meshed rather easily using 4-node quadrilateral elements, but then in general practical analysis quite distorted elements might be present that show low predictive capabilities. Namely, quadrilateral elements generally do not perform well when highly distorted.

It is difficult to develop effective shell finite elements that give reliable and efficient solutions for general shell problems, when considering the various shell geometries, boundary and loading conditions, and mesh patterns used [2–4]. The difficulty is basically due to the highly sensitive and complex behavior of shell structures (categorized as bending dominated, membrane dominated and mixed behaviors), in particular, when the shell thickness is small [3,4]. Then a shell finite element discretization frequently gives too stiff solutions. This phenomenon is called "locking", which must be alleviated for reliable shell finite element analysis. Among various schemes to alleviate the locking, the MITC (Mixed Interpolation of Tensorial Components) scheme has been used very successfully in the development of general shell elements [1–7].

The MITC3+ shell element is based on the concepts of the MITC3 shell element developed by Lee and Bathe [6] with an enrichment by a cubic bubble function for the rotations. The cubic bubble function provides a higher-order interpolation inside the element to enrich the element behavior while maintaining the linear interpolation along the element edges. The degrees of freedom corresponding to the bubble function can be statically condensed out on the element level. To alleviate shear locking, a newly developed assumed transverse shear strain field is used. The shell element passes the basic numerical tests – the isotropy, zero energy mode and patch tests – and shows an excellent convergence behavior in linear analysis.

A particular strength of the MITC approach is that a formulation achieved for linear analysis can be directly extended to nonlinear analysis by "simply" using the appropriate stress and strain measures [2], although the performance in nonlinear solutions must then of course still be studied.

Our objective in this paper is to present the formulation of the MITC3+ shell element in geometric nonlinear analysis. The standard total Lagrangian formulation is employed allowing for large

* Corresponding author.
E-mail address: phillseung@kaist.edu (P.S. Lee).

http://dx.doi.org/10.1016/j.compstruc.2014.09.004
0045-7949/

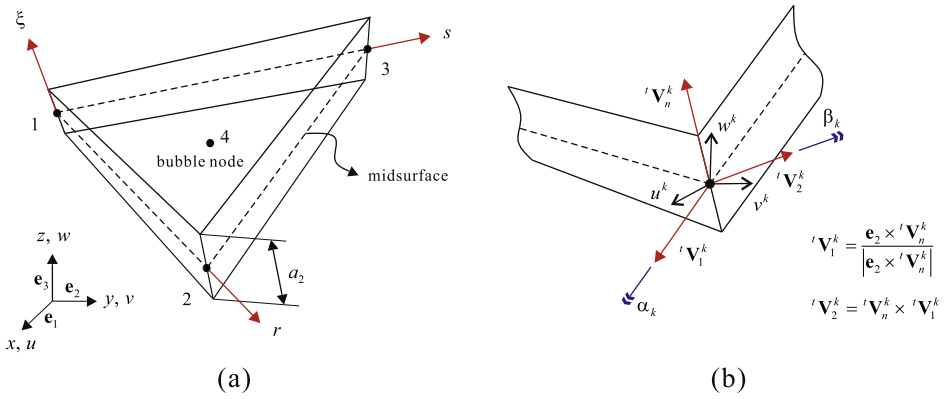

Fig. 1. The MITC3+ shell finite element with the bubble node: (a) Geometry of the MITC3+ shell finite element. (b) Definition of rotational degrees of freedom α_k and β_k. In linear analysis the superscript t is not used.

displacements and large rotations [2]. Solving various shell problems, the performance of the MITC3+ shell element is evaluated by comparison of the solution accuracies obtained with the MITC3+, MITC3 and MITC4 shell elements. Of course, the MITC4 quadrilateral shell element has been, and is, widely employed in engineering practice due to its superior performance in both linear and nonlinear analyses. Our study reveals that the performance of the MITC3+ shell element in nonlinear analysis is as good as the performance of the MITC4 shell element, even when highly distorted meshes are used.

Next, in Section 2, the linear formulation of the MITC3+ shell element is reviewed and, in Section 3, we present the geometric nonlinear formulation. In Section 4, we examine the performance of the MITC3+ shell element in geometric nonlinear analysis through the solutions of various shell problems.

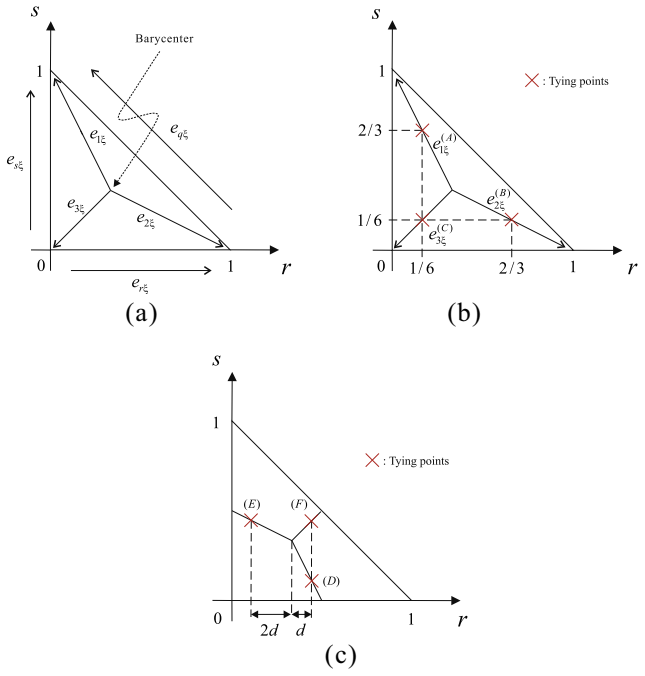

Fig. 2. Transverse shear strains $e_{1\xi}$, $e_{2\xi}$ and $e_{3\xi}$, and the tying positions (A), (B), (C), (D), (E) and (F) for the assumed transverse shear strain field.

Table 1
Tying positions for the assumed transverse shear strain for the MITC3+ shell elements. The distance d is defined in Fig. 2(c), and $d = 1/10{,}000$ is used [1].

	Tying position	r	s
Fig. 2(b)	(A)	1/6	2/3
	(B)	2/3	1/6
	(C)	1/6	1/6
Fig. 2(c)	(D)	$1/3 + d$	$1/3 - 2d$
	(E)	$1/3 - 2d$	$1/3 + d$
	(F)	$1/3 + d$	$1/3 + d$

2. The MITC3+ shell element for linear analysis

In this section, we briefly review the formulation of the MITC3+ shell element for linear analysis [1]. The two key aspects of the MITC3+ shell element are the geometry and displacement interpolations and the assumed covariant transverse shear strain fields.

2.1. Geometry and displacement interpolations

The geometry interpolation of the MITC3+ shell element, shown in Fig. 1, is given by

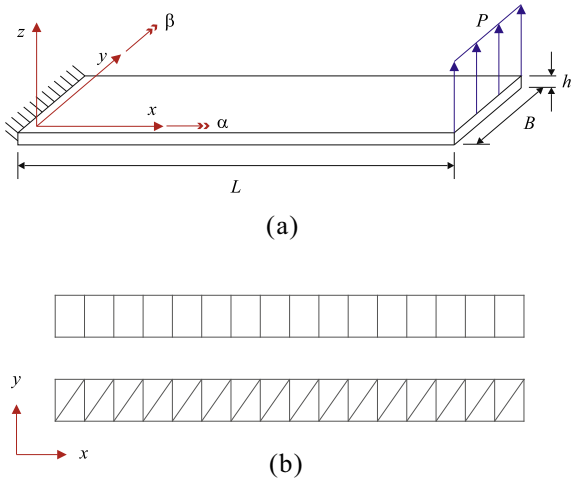

Fig. 3. Cantilever plate subjected to end shear force. (a) Problem description. (b) Meshes used for the MITC4 (top), MITC3 and MITC3+ (bottom) shell elements.

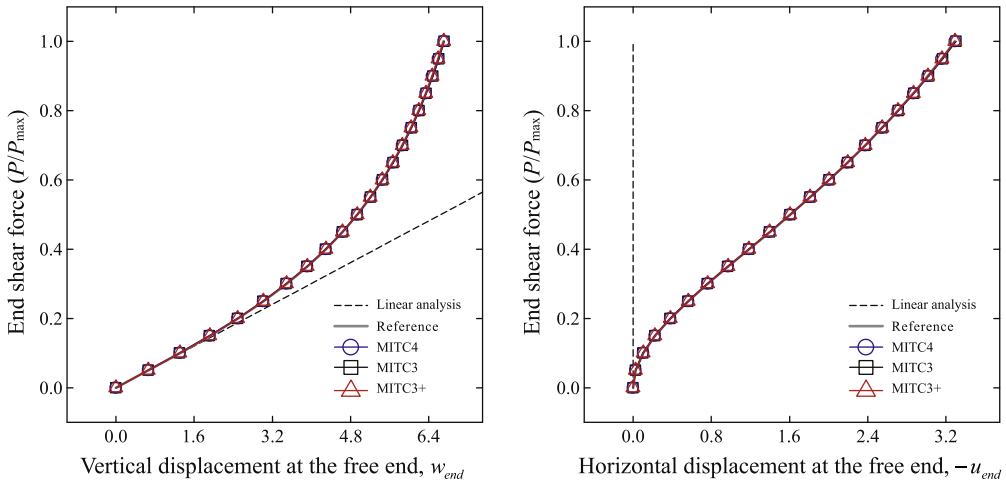

Fig. 4. Load–displacement curves for the cantilever plate subjected to end shear force. For the triangular element meshes, essentially the same response is measured at the two corners.

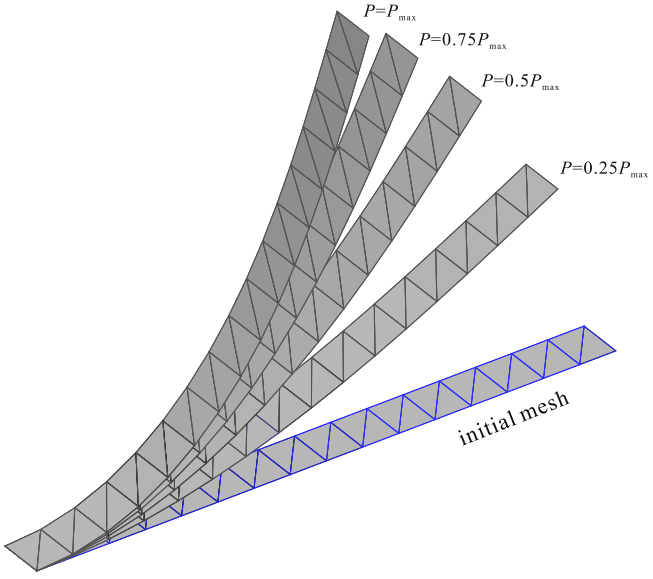

Fig. 5. Deformed configurations of the cantilever plate under end shear force.

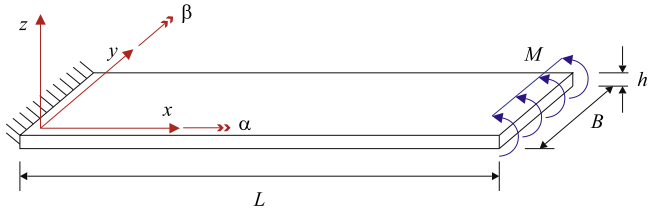

Fig. 6. Cantilever plate subjected to end moment.

$$\mathbf{x}(r,s,\xi)=\sum_{i=1}^{3}h_i(r,s)\mathbf{x}_i+\frac{\xi}{2}\sum_{i=1}^{4}a_i f_i(r,s)\mathbf{V}_n^i$$

with $h_1=1-r-s,\ h_2=r,\ h_3=s,$

$$a_4\mathbf{V}_n^4=\frac{1}{3}\left(a_1\mathbf{V}_n^1+a_2\mathbf{V}_n^2+a_3\mathbf{V}_n^3\right), \tag{1}$$

in which $h_i(r,s)$ is the two-dimensional interpolation function of the standard isoparametric procedure corresponding to node i, $\mathbf{x}_i$ is the position vector of node i in the global Cartesian coordinate system, a_i and $\mathbf{V}_n^i$ denote the shell thickness and the director vector at node i, respectively, and $f_i(r,s)$ are the two-dimensional interpolation functions that include the cubic bubble function f_4 corresponding to the internal node 4

$$f_1=h_1-\frac{1}{3}f_4,\quad f_2=h_2-\frac{1}{3}f_4,\quad f_3=h_3-\frac{1}{3}f_4,$$
$$f_4=27rs(1-r-s). \tag{2}$$

Unlike the standard 3-node shell elements, the MITC3+ shell element has an internal node and the corresponding cubic bubble function in the geometry interpolation.

From Eq. (1), the displacement interpolation of the MITC3+ shell element for linear analysis is obtained by [1]

$$\mathbf{u}(r,s,\xi)=\sum_{i=1}^{3}h_i(r,s)\mathbf{u}_i+\frac{\xi}{2}\sum_{i=1}^{4}a_i f_i(r,s)\left(-\mathbf{V}_2^i\alpha_i+\mathbf{V}_1^i\beta_i\right), \tag{3}$$

in which $\mathbf{u}_i$ is the nodal displacement vector in the global Cartesian coordinate system, $\mathbf{V}_1^i$ and $\mathbf{V}_2^i$ are the unit vectors orthogonal to $\mathbf{V}_n^i$ and to each other, and α_i and β_i are the rotations of the director vector $\mathbf{V}_n^i$ about $\mathbf{V}_1^i$ and $\mathbf{V}_2^i$, respectively, at node i.

The interior node, with rotation degrees of freedom only, is positioned on the flat surface defined by the three corner nodes of the element. Only the bending and transverse shear strain fields are enriched by the bubble function, and the geometry of the element remains flat, as for the MITC3 element, in a large deformation analysis. Of course, static condensation can be carried out on the element level for the rotations α_4 and β_4, and hence in practice the element is really a 3-node element.

2.2. Assumed covariant transverse shear strain fields

For linear analysis, the linear part of the Green–Lagrange strain tensor is used and its covariant strain components are

$$e_{ij}=\frac{1}{2}\left(\mathbf{g}_i\cdot\mathbf{u}_{,j}+\mathbf{g}_j\cdot\mathbf{u}_{,i}\right), \tag{4}$$

in which

$$\mathbf{g}_i=\frac{\partial\mathbf{x}}{\partial r_i},\quad \mathbf{u}_{,i}=\frac{\partial\mathbf{u}}{\partial r_i}\quad \text{with } r_1=r,\ r_2=s,\ r_3=\xi. \tag{5}$$

Since the MITC3+ shell element is flat, the covariant in-plane strain components are directly calculated using Eqs. (1)–(5). How-

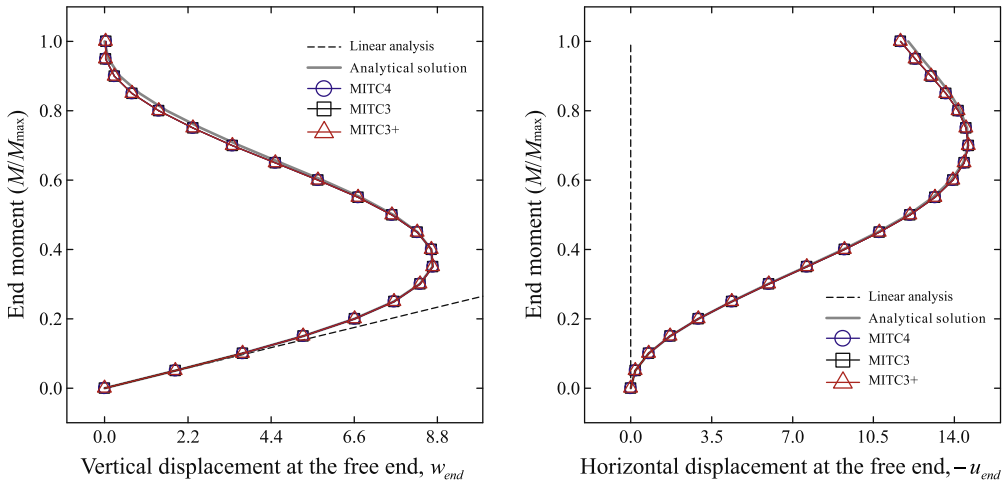

Fig. 7. Load–displacement curves for the cantilever plate subjected to end moment. For the triangular element meshes, essentially the same response is measured at the two corners.

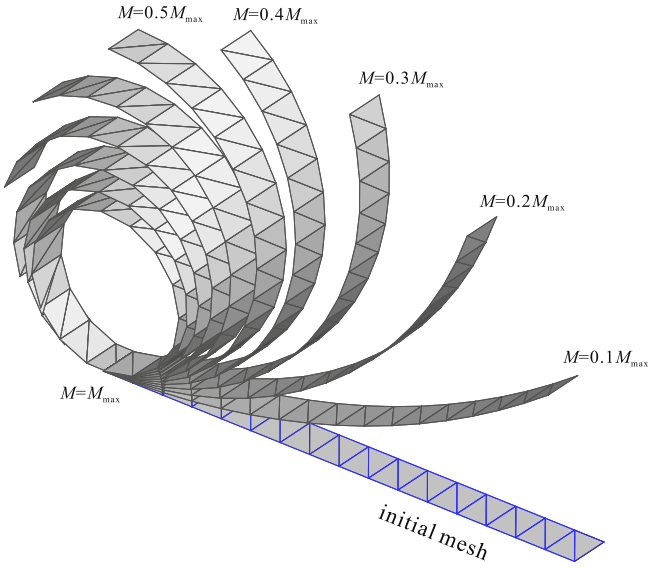

Fig. 8. Deformed configurations of the cantilever plate under end moment.

ever, the covariant transverse shear strain fields are established using the MITC scheme to alleviate shear locking. The assumed transverse shear strain fields of the MITC3+ shell element are given by

$$e^{AS}_{r_\xi} = \frac{2}{3}\left(e^{(B)}_{r_\xi} - \frac{1}{2}e^{(B)}_{s_\xi}\right) + \frac{1}{3}\left(e^{(C)}_{r_\xi} + e^{(C)}_{s_\xi}\right) + \frac{1}{3}\hat{c}(3s-1),$$

$$e^{AS}_{s_\xi} = \frac{2}{3}\left(e^{(A)}_{s_\xi} - \frac{1}{2}e^{(A)}_{r_\xi}\right) + \frac{1}{3}\left(e^{(C)}_{r_\xi} + e^{(C)}_{s_\xi}\right) + \frac{1}{3}\hat{c}(1-3r), \tag{6}$$

where $\hat{c} = e^{(F)}_{r_\xi} - e^{(D)}_{r_\xi} - e^{(F)}_{s_\xi} + e^{(E)}_{s_\xi}$ and the tying positions (A), (B), (C), (D), (E), and (F) are presented in Fig. 2 and Table 1. We use $d = 1/10{,}000$ as suggested [1]. If $d = 0$ is used, there is one spurious zero eigenvalue for a single element, which however disappears as soon as two elements are used in the mesh.

The MITC3+ shell element is based on the 'basic mathematical shell model' [4,8,9] and the MITC scheme. The element passes the basic numerical tests, namely, the isotropy, zero energy mode, and patch tests. Furthermore, the MITC3+ shell element shows an excellent convergence behavior in both membrane and bending dominated shell problems, even when distorted meshes are used [1].

3. The MITC3+ shell element for geometric nonlinear analysis

In this section, we present the geometric nonlinear formulation of the MITC3+ shell element. The total Lagrangian formulation is employed allowing for large displacements and large rotations. In the formulation, a superscript (and subscript) t is used to denote "time" for general analysis, with in static solutions "time" simply denoting the load step and configuration [2].

We discuss below the large displacement kinematics and the interpolation of the Green–Lagrange strain components. With the given expressions, the now classical incremental equations used in the total Lagrangian formulation can directly be established [2].

3.1. Large displacement kinematics

The geometry of the MITC3+ shell finite element in the configuration at time t shown in Fig. 1 is interpolated with

$${}^t\mathbf{x}(r,s,\xi) = \sum_{i=1}^{3} h_i(r,s)\,{}^t\mathbf{x}_i + \frac{\xi}{2}\sum_{i=1}^{4} a_i f_i(r,s)\,{}^t\mathbf{V}^i_n, \tag{7}$$

in which ${}^t\mathbf{x}_i$ is the position vector of node i in the configuration at time t, and ${}^t\mathbf{V}^i_n$ denotes the director vector at node i in the configuration at time t.

The incremental displacements from the configuration at time t to the configuration at time $t + \Delta t$ are

$$\mathbf{u}(r,s,\xi) = {}^{t+\Delta t}\mathbf{x}(r,s,\xi) - {}^t\mathbf{x}(r,s,\xi), \tag{8}$$

and hence

$$\mathbf{u}(r,s,\xi) = \sum_{i=1}^{3} h_i(r,s)\mathbf{u}_i + \frac{\xi}{2}\sum_{i=1}^{4} a_i f_i(r,s)\left({}^{t+\Delta t}\mathbf{V}^i_n - {}^t\mathbf{V}^i_n\right), \tag{9}$$

where $\mathbf{u}_i$ is the vector of incremental nodal displacements at node i from time t to time $t + \Delta t$. Note that $\mathbf{u}(r,s,\xi)$ is the displacement vector in the linear formulation, see Eq. (3), but here it is the vector of incremental displacements.

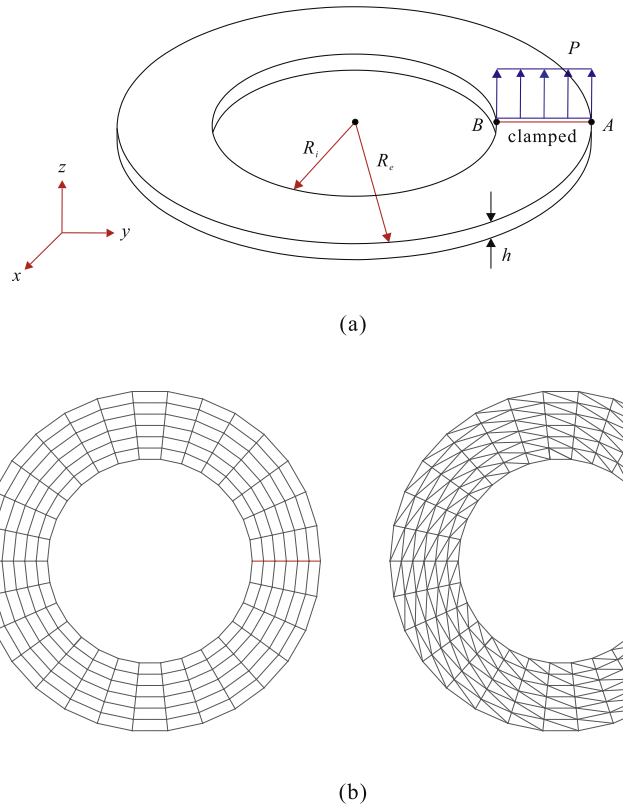

Fig. 9. Slit annular plate under end shear force. (a) Problem description. (b) Meshes used.

The director vector at time $t + \Delta t$ at node i is obtained from the director vector at time t

$$ {}^{t+\Delta t}\mathbf{V}_n^i = {}^{t+\Delta t}_{t}\mathbf{Q}^{\,i}\ {}^{t}\mathbf{V}_n^i, \tag{10} $$

in which ${}^{t+\Delta t}_{t}\mathbf{Q}^{\,i}$ is the rotation matrix which rotates the director vector at node i from the configuration at time t to the configuration at time $t + \Delta t$. Additionally, the two unit vectors ${}^{t}\mathbf{V}_1^i$ and ${}^{t}\mathbf{V}_2^i$ are obtained by (see Fig. 1(b)),

$$ {}^{t}\mathbf{V}_1^i = \frac{\mathbf{e}_2 \times {}^{t}\mathbf{V}_n^i}{\left|\mathbf{e}_2 \times {}^{t}\mathbf{V}_n^i\right|}, \quad {}^{t}\mathbf{V}_2^i = {}^{t}\mathbf{V}_n^i \times {}^{t}\mathbf{V}_1^i. \tag{11} $$

For the vector-like parameterization of finite rotations [2,10], we employ the well-known formula

$$ {}^{t+\Delta t}_{t}\mathbf{Q}^{\,i} = \mathbf{I}_3 + \frac{\sin\left({}^{t+\Delta t}_{t}\theta^i\right)}{{}^{t+\Delta t}_{t}\theta^i}\,{}^{t+\Delta t}_{t}\mathbf{\Theta}^i + \frac{1}{2}\left[\frac{\sin\left({}^{t+\Delta t}_{t}\theta^i/2\right)}{{}^{t+\Delta t}_{t}\theta^i/2}\right]^2 \left({}^{t+\Delta t}_{t}\mathbf{\Theta}^i\right)^2 \tag{12} $$

with

$$ {}^{t+\Delta t}_{t}\mathbf{\Theta}^i = \begin{bmatrix} 0 & -{}^{t+\Delta t}_{t}\theta_3^i & {}^{t+\Delta t}_{t}\theta_2^i \\ {}^{t+\Delta t}_{t}\theta_3^i & 0 & -{}^{t+\Delta t}_{t}\theta_1^i \\ -{}^{t+\Delta t}_{t}\theta_2^i & {}^{t+\Delta t}_{t}\theta_1^i & 0 \end{bmatrix}, \tag{13} $$

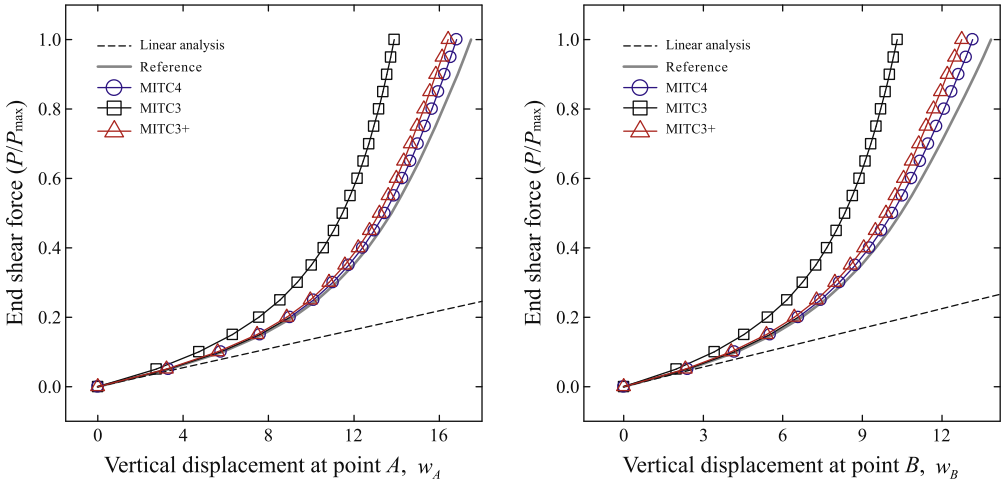

Fig. 10. Load–displacement curves for the slit annular plate under end shear force.

$$ {}^{t+\Delta t}_{t}\boldsymbol{\theta}^{i} = \alpha_i {}^{t}\mathbf{V}_1^{i} + \beta_i {}^{t}\mathbf{V}_2^{i}, \tag{14} $$

in which $\mathbf{I}_3$ is the 3×3 identity matrix, ${}^{t+\Delta t}_{t}\boldsymbol{\Theta}^{i}$ is the skew-symmetric matrix operator, ${}^{t+\Delta t}_{t}\boldsymbol{\theta}^{i} = [{}^{t+\Delta t}_{t}\theta_1^{i} \quad {}^{t+\Delta t}_{t}\theta_2^{i} \quad {}^{t+\Delta t}_{t}\theta_3^{i}]^{T}$, and ${}^{t+\Delta t}_{t}\theta^{i} = \sqrt{({}^{t+\Delta t}_{t}\theta_1^{i})^2 + ({}^{t+\Delta t}_{t}\theta_2^{i})^2 + ({}^{t+\Delta t}_{t}\theta_3^{i})^2}$.

Using a Taylor series expansion, the finite rotation tensor ${}^{t+\Delta t}_{t}\mathbf{Q}^{i}$ can be represented by

$$ {}^{t+\Delta t}_{t}\mathbf{Q}^{i} = \mathbf{I}_3 + {}^{t+\Delta t}_{t}\boldsymbol{\Theta}^{i} + \frac{1}{2!}\left({}^{t+\Delta t}_{t}\boldsymbol{\Theta}^{i}\right)^2 + \frac{1}{3!}\left({}^{t+\Delta t}_{t}\boldsymbol{\Theta}^{i}\right)^3 + \cdots\cdots. \tag{15} $$

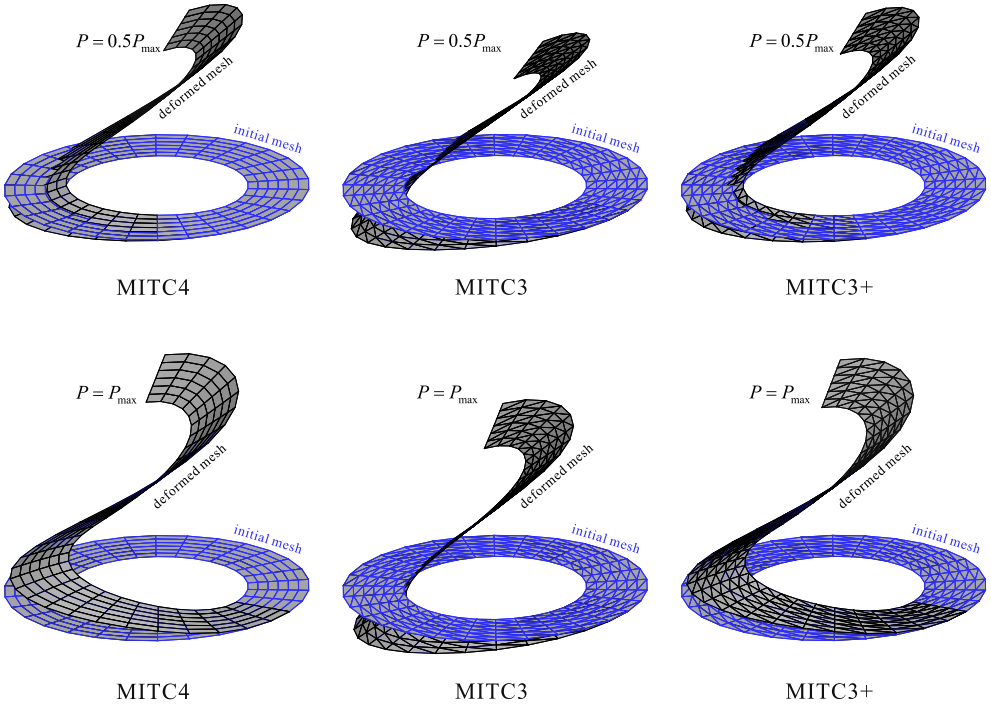

Fig. 11. Deformed configurations of the slit annular plate under end shear force.

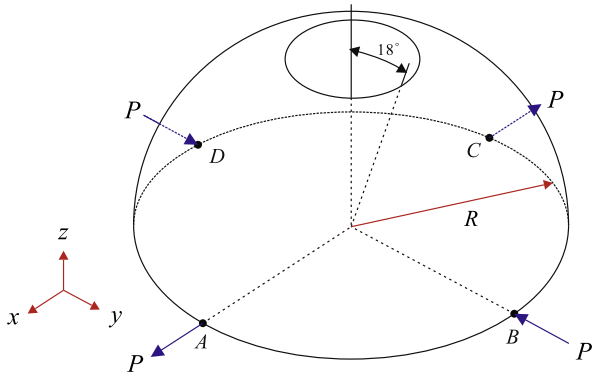

(a)

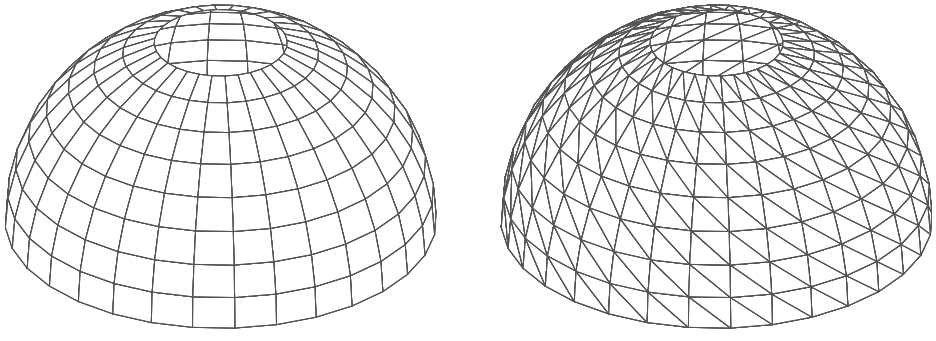

(b)

Fig. 12. Hemispherical shell subjected to alternating radial forces. (a) Problem solved. (b) Meshes used (8×32).

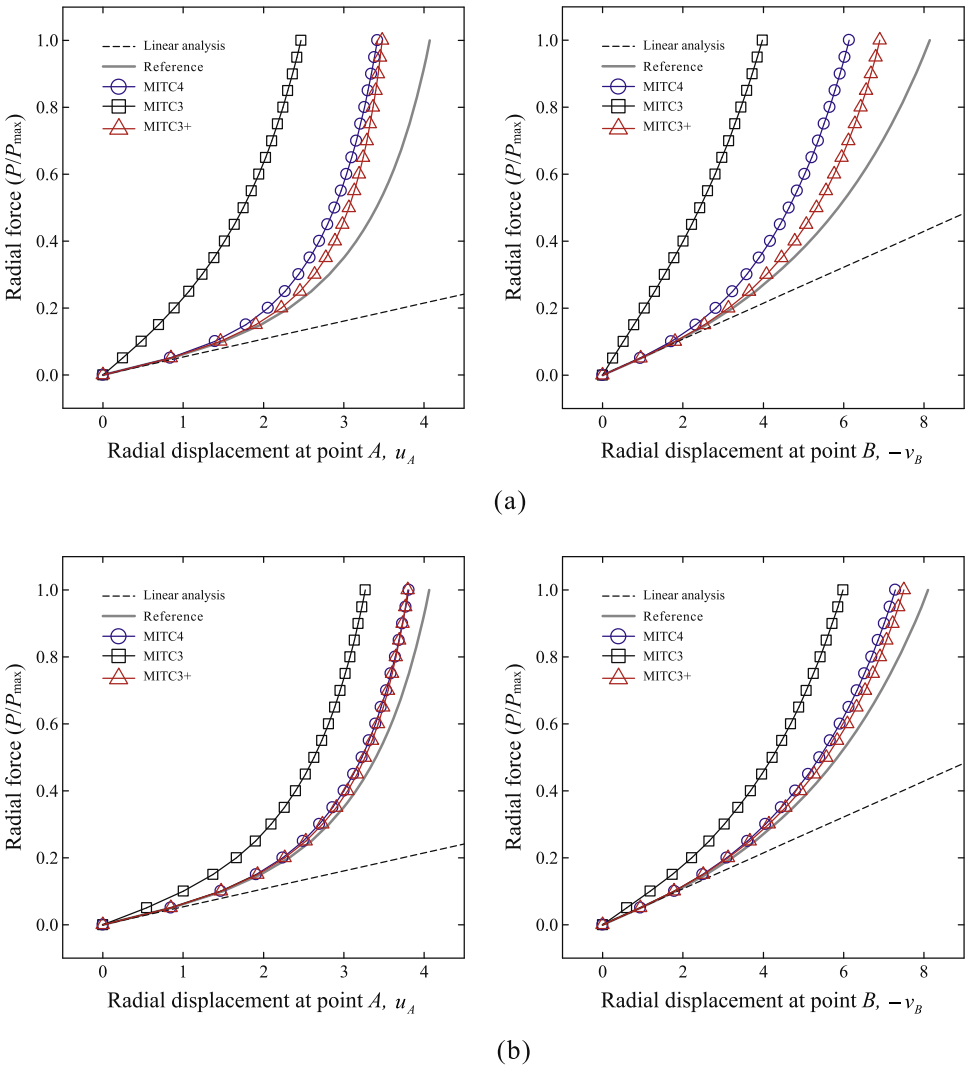

Fig. 13. Load–displacement curves for the hemispherical shell subjected to alternating radial forces when (a) 8 × 32 and (b) 12 × 48 element meshes are used.

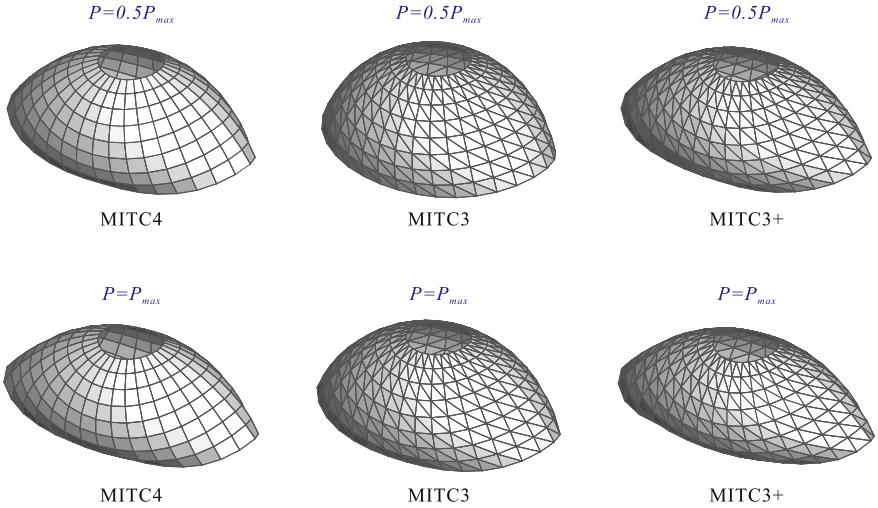

Fig. 14. Deformed configurations of the hemispherical shell subjected to alternating radial forces.

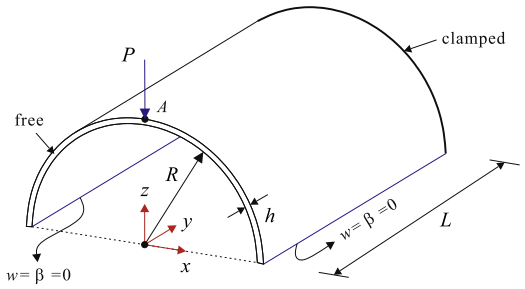

(a)

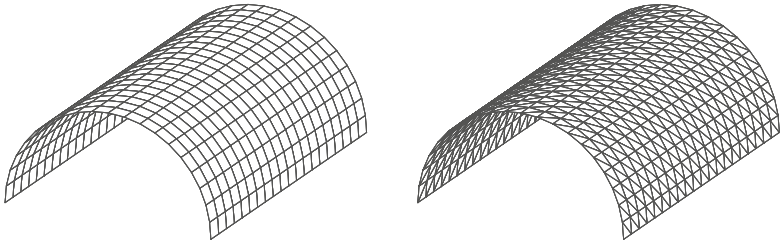

(b)

Fig. 15. Clamped semi-cylindrical shell under point load. (a) Problem description (b) Meshes used (20 × 20).

Using only the terms up to quadratic order in Eq. (15), the following equation is obtained

$$ {}^{t+\Delta t}\mathbf{V}_n^i - {}^{t}\mathbf{V}_n^i = {}^{t+\Delta t}_{t}\boldsymbol{\theta}^i \times {}^{t}\mathbf{V}_n^i + \frac{1}{2}{}^{t+\Delta t}_{t}\boldsymbol{\theta}^i \times ({}^{t+\Delta t}_{t}\boldsymbol{\theta}^i \times {}^{t}\mathbf{V}_n^i), \tag{16} $$

and using Eq. (14) in Eq. (16), we obtain for a 'consistent linearization' of the element displacements [2]

$$ {}^{t+\Delta t}\mathbf{V}_n^i - {}^{t}\mathbf{V}_n^i = -\alpha_i {}^{t}\mathbf{V}_2^i + \beta_i {}^{t}\mathbf{V}_1^i - \frac{1}{2}(\alpha_i{}^2 + \beta_i^2){}^{t}\mathbf{V}_n^i. \tag{17} $$

Substituting Eq. (17) into Eq. (9), the vector of incremental displacements including second-order rotation effects is

$$ \mathbf{u}(r,s,\xi) = \sum_{i=1}^{3} h_i(r,s)\mathbf{u}_i + \frac{\xi}{2}\sum_{i=1}^{4} a_i f_i(r,s)\left[-\alpha_i {}^{t}\mathbf{V}_2^i + \beta_i {}^{t}\mathbf{V}_1^i - \frac{1}{2}(\alpha_i{}^2 + \beta_i^2){}^{t}\mathbf{V}_n^i\right], \tag{18} $$

in which α_i and β_i are the incremental rotations of the director vector ${}^{t}\mathbf{V}_n^i$ about ${}^{t}\mathbf{V}_1^i$ and ${}^{t}\mathbf{V}_2^i$, respectively, at node i.

Note that the incremental displacement in Eq. (18) consists of two parts, the linear part $\mathbf{u}_l$ and the quadratic part $\mathbf{u}_q$, hence

$$ \mathbf{u}(r,s,\xi) = \mathbf{u}_l(r,s,\xi) + \mathbf{u}_q(r,s,\xi), \tag{19} $$

with

$$ \mathbf{u}_l(r,s,\xi) = \sum_{i=1}^{3} h_i(r,s)\mathbf{u}_i + \frac{\xi}{2}\sum_{i=1}^{4} a_i f_i(r,s)\left(-\alpha_i {}^{t}\mathbf{V}_2^i + \beta_i {}^{t}\mathbf{V}_1^i\right), \tag{20} $$

and

$$ \mathbf{u}_q(r,s,\xi) = -\frac{\xi}{4}\sum_{i=1}^{4} a_i f_i(r,s)\left[(\alpha_i{}^2 + \beta_i^2){}^{t}\mathbf{V}_n^i\right]. \tag{21} $$

3.2. Green–Lagrange strain and its interpolation

The covariant components of the Green–Lagrange strain tensor in the configuration at time t, referred to the configuration at time 0, are defined by [2]

$$ {}^{t}_{0}\varepsilon_{ij} = \frac{1}{2}\left({}^{t}\mathbf{g}_i \cdot {}^{t}\mathbf{g}_j - {}^{0}\mathbf{g}_i \cdot {}^{0}\mathbf{g}_j\right) \quad \text{with} \quad {}^{0}\mathbf{g}_i = \frac{\partial {}^{0}\mathbf{x}}{\partial r_i},\ {}^{t}\mathbf{g}_i = \frac{\partial {}^{t}\mathbf{x}}{\partial r_i} = {}^{0}\mathbf{g}_i + {}^{t}\mathbf{u}_{,i}, \tag{22} $$

$$ \text{in which} \quad {}^{t}\mathbf{u}_{,i} = \frac{\partial {}^{t}\mathbf{u}}{\partial r_i},\ {}^{t}\mathbf{u} = {}^{t}\mathbf{x} - {}^{0}\mathbf{x},\ r_1 = r,\ r_2 = s,\ r_3 = \xi. \tag{23} $$

Hence the incremental covariant strains are

$$ {}_{0}\varepsilon_{ij} = {}^{t+\Delta t}_{0}\varepsilon_{ij} - {}^{t}_{0}\varepsilon_{ij} = \frac{1}{2}\left(\mathbf{u}_{,i} \cdot {}^{t}\mathbf{g}_j + {}^{t}\mathbf{g}_i \cdot \mathbf{u}_{,j} + \mathbf{u}_{,i} \cdot \mathbf{u}_{,j}\right) \quad \text{with} \quad \mathbf{u}_{,i} = \frac{\partial \mathbf{u}}{\partial r_i}. \tag{24} $$

Using Eq. (19) in Eq. (24), these strains are approximated as

$$ {}_{0}\varepsilon_{ij} = {}_{0}e_{ij} + {}_{0}\eta_{ij}, \tag{25} $$

where ${}_{0}e_{ij}$ and ${}_{0}\eta_{ij}$ are the linear and nonlinear parts, respectively,

$$ {}_{0}e_{ij} = \frac{1}{2}\left(\frac{\partial \mathbf{u}_l}{\partial r_i} \cdot {}^{t}\mathbf{g}_j + {}^{t}\mathbf{g}_i \cdot \frac{\partial \mathbf{u}_l}{\partial r_j}\right) = \mathbf{B}_{ij}\mathbf{U}, \tag{26} $$

$$ {}_{0}\eta_{ij} = \frac{1}{2}\left(\frac{\partial \mathbf{u}_l}{\partial r_i} \cdot \frac{\partial \mathbf{u}_l}{\partial r_j}\right) + \frac{1}{2}\left(\frac{\partial \mathbf{u}_q}{\partial r_i} \cdot {}^{t}\mathbf{g}_j + {}^{t}\mathbf{g}_i \cdot \frac{\partial \mathbf{u}_q}{\partial r_j}\right) = \frac{1}{2}\mathbf{U}^T\mathbf{N}_{ij}\mathbf{U}, \tag{27} $$

in which $\mathbf{B}_{ij}$ and $\mathbf{N}_{ij}$ are the strain–displacement matrices and $\mathbf{U}$ is the vector of incremental nodal displacements and rotations $\mathbf{u}_i$, α_i and β_i for all element nodes. In addition, the strain variations are

$$ \delta_0 e_{ij} = \mathbf{B}_{ij}\delta\mathbf{U}, \quad \delta_0\eta_{ij} = \delta\mathbf{U}^T\mathbf{N}_{ij}\mathbf{U}. \tag{28} $$

Note that Eqs. (25)–(28) contain all the strain terms to have a consistent linearization in the establishment of the tangent stiffness matrix.

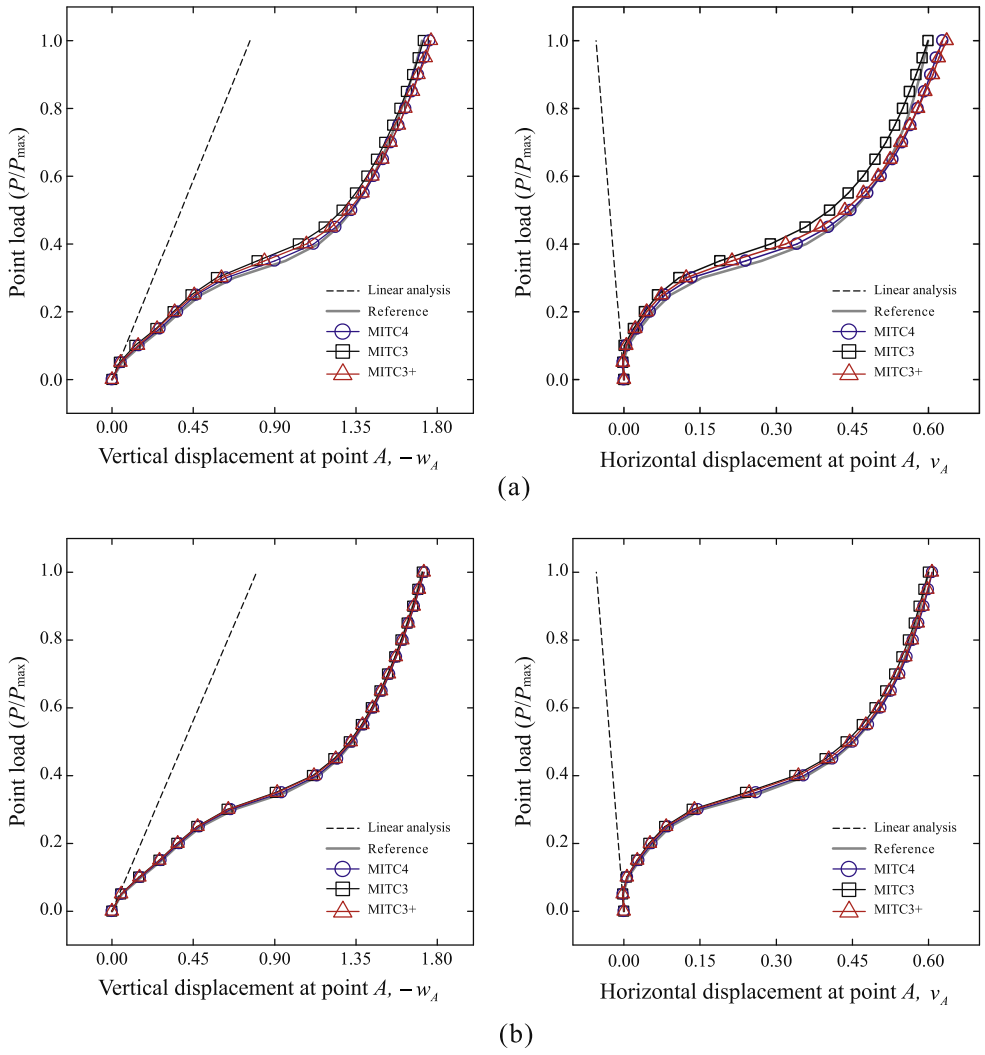

Fig. 16. Load–displacement curves for the clamped semi-cylindrical shell under point load when (a) 20×20 and (b) 32×32 element meshes are used.

To alleviate shear locking, the MITC scheme used in the linear formulation of the MITC3+ shell element is also employed for the incremental covariant transverse shear strains in the nonlinear formulation. Therefore, the covariant transverse shear strains in Eqs. (25)–(28) are substituted by

$$ {}_0\varepsilon^{AS}_{r\xi} = \frac{2}{3}\left({}_0\varepsilon^{(B)}_{r\xi} - \frac{1}{2}{}_0\varepsilon^{(B)}_{s\xi}\right) + \frac{1}{3}\left({}_0\varepsilon^{(C)}_{r\xi} + {}_0\varepsilon^{(C)}_{s\xi}\right) + \frac{1}{3}{}_0\hat{c}(3s-1), \tag{29} $$

$$ {}_0\varepsilon^{AS}_{s\xi} = \frac{2}{3}\left({}_0\varepsilon^{(A)}_{s\xi} - \frac{1}{2}{}_0\varepsilon^{(A)}_{r\xi}\right) + \frac{1}{3}\left({}_0\varepsilon^{(C)}_{r\xi} + {}_0\varepsilon^{(C)}_{s\xi}\right) + \frac{1}{3}{}_0\hat{c}(1-3r), \tag{30} $$

$$ {}_0\varepsilon^{AS}_{j\xi} = {}_0e^{AS}_{j\xi} + {}_0\eta^{AS}_{j\xi}, \quad {}_0e^{AS}_{j\xi} = \mathbf{B}^{AS}_{j\xi}\mathbf{U}, \quad {}_0\eta^{AS}_{j\xi} = \frac{1}{2}\mathbf{U}^T\mathbf{N}^{AS}_{j\xi}\mathbf{U} \quad \text{with} \quad j = r,s \tag{31} $$

in which ${}_0\hat{c} = {}_0\varepsilon^{(F)}_{r\xi} - {}_0\varepsilon^{(D)}_{r\xi} - {}_0\varepsilon^{(F)}_{s\xi} + {}_0\varepsilon^{(E)}_{s\xi}$, $\mathbf{B}^{AS}_{j\xi}$ and $\mathbf{N}^{AS}_{j\xi}$ are the strain–displacement matrices for the assumed covariant transverse shear strains. Of course, the tying positions defined in Fig. 2 and Table 1 are used.

For the evaluation of the element stiffness matrix and internal nodal force vector, we use 7-point Gauss integration in the r–s plane (as for the MITC6 shell element) due to the cubic bubble function. Hence, since also 6 tying points and the fourth node are used, compared to the MITC3 shell element (using 3 tying points and 3-point Gauss integration), the MITC3+ shell element requires for the evaluation of these element quantities clearly more computational time.

4. Numerical examples

To assess the performance of the MITC3+ shell element in geometric nonlinear analysis, the solutions of several benchmark problems are given in this section. The problems involve the large displacement and large rotation response of shells with various shell geometries. The results calculated using the following MITC shell elements are given

- MITC3: 3-node triangular shell element
- MITC3+: 3-node triangular shell element enriched by a cubic bubble function (presented in this paper)
- MITC4: 4-node quadrilateral shell element

In each example, the reference solutions are given by either an analytical result or a calculated solution using a fine uniform mesh of the MITC9 shell element (these meshes used twice the number of elements in each direction as employed in the MITC4 element solutions) [11]. The MITC9 element is known to satisfy the ellipticity and consistency conditions and to show good convergence behavior [5,11,12]. For comparison, we also plot the results of the linear analysis calculated using the MITC9 shell element. The

iterations to solve the nonlinear equations have been performed in each load step to a convergence tolerance of 0.1 percent on the relative incremental energy.

Note that in some benchmark problems, point loads are used, which cause a stress singularity at the point of loading. However, the use of point loads is acceptable in the studies here given because the meshes are not very fine (the point loads act as an equivalent pressure applied over a small area) [2].

4.1. Cantilever plate subjected to end shear force

The cantilever plate shown in Fig. 3(a) is subjected to a shear force at the free end. This problem has been considered many times before, see e.g. [13-15]. The material properties, geometry and applied force are chosen as $E = 1.2 \times 10^6$, $\nu = 0$, $L = 10$, $B = 1$, $h = 0.1$ and $P_{max} = 4$. Fig. 3(b) shows the 16×1 mesh used for the solution with the MITC4 shell element and the corresponding mesh used for the MITC3 and MITC3+ shell elements. The reference solutions are calculated using a 32×2 element mesh of the MITC9 shell element.

Fig. 4 shows the calculated load–displacement curves. Fig. 5 depicts the deformed configurations of the cantilever plate obtained using the MITC3+ shell element at various load levels ($P = 0.25P_{max}$, $0.5P_{max}$, $0.75P_{max}$, and P_{max}). All shell elements considered show excellent performance in the solution of this problem.

4.2. Cantilever plate subjected to end moment

Fig. 6 shows the cantilever plate subjected to a moment at the free end. This is a good problem to test the large rotation capability of shell elements [16-19]. The cantilever plate has length $L = 12$, width $B = 1$, thickness $h = 0.1$, Young's modulus $E = 1.2 \times 10^6$ and Poisson's ratio $\nu = 0$. We use the end moment $M_{max} = 2\pi M_0$ with $M_0 = EI/L$, and hence the cantilever rolls up into a complete circle. The structure is modeled using a 16×1 element mesh of the

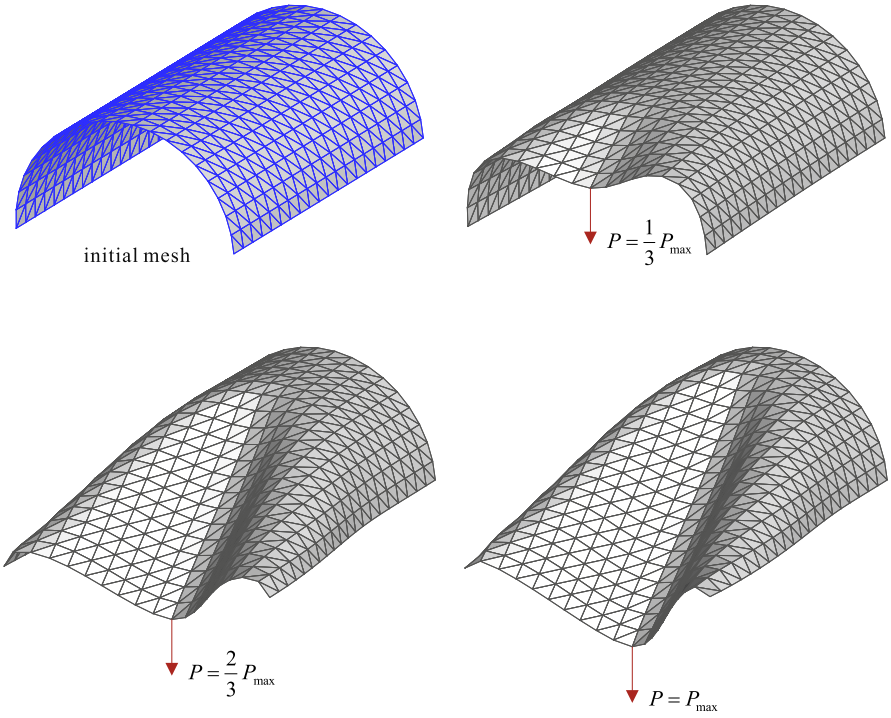

Fig. 17. Deformed configurations of the clamped semi-cylindrical shell under point load.

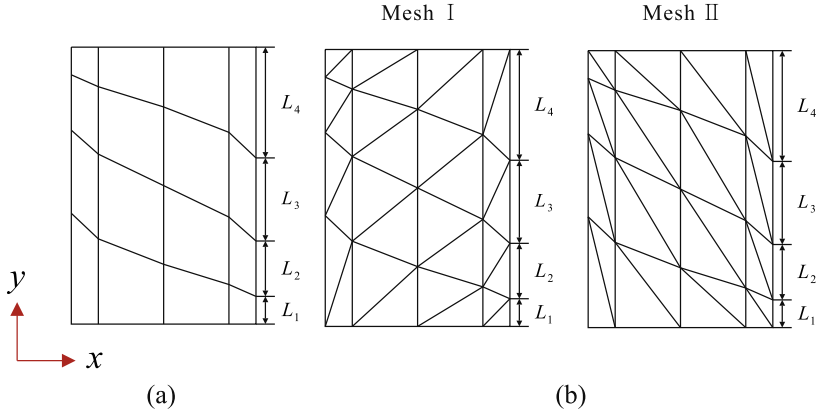

Fig. 18. Distorted mesh patterns of the clamped semi-cylindrical shell ($N = 4$) (a) for the MITC4 shell element and (b) for the MITC3 and MITC3+ shell elements.

MITC4 shell element and the corresponding MITC3 and MITC3+ shell element meshes, see Fig. 3(b). The reference solutions are calculated using a 32×2 element mesh of the MITC9 shell element.

The cantilever forms a circular arc of radius R given by the classical formula $R = EI/M$. Thus, the analytical tip displacements are derived as

$$\frac{U}{L} = \frac{M_0}{M}\sin\left(\frac{M}{M_0}\right) - 1, \quad \frac{W}{L} = \frac{M_0}{M}\left(1 - \cos\frac{M}{M_0}\right). \tag{32}$$

Fig. 7 depicts the calculated load–displacement curves and Fig. 8 shows successive deformed configurations calculated using the MITC3+ shell element at various load stages ($M = 0.1M_{\max}$, $0.2M_{\max}, 0.3M_{\max}, \ldots, M_{\max}$). All computed results show good agreement with the analytical solutions.

4.3. Slit annular plate under end shear force

We examine here a slit annular plate, as shown in Fig. 9(a). This example was suggested by Başar and Ding [20] and has been widely considered [16,19,21-25]. The geometry and elastic material properties are given by $R_i = 6$, $R_e = 10$, $h = 0.03$, $E = 21 \times 10^6$ and $\nu = 0$. The transverse shear force $P_{\max} = 3.2$ is incrementally applied at one end of the slit while the other end of the slit is fully clamped. The plate undergoes large displacements and large

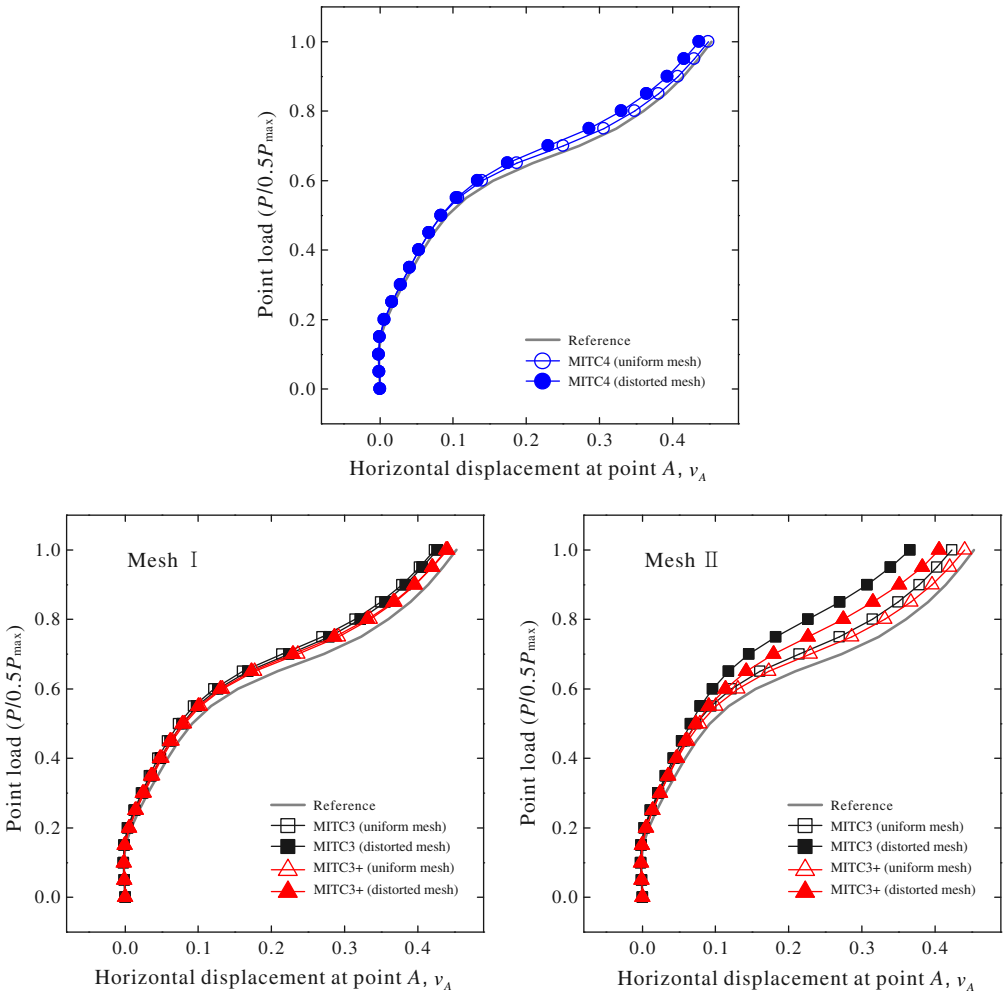

Fig. 19. Load–displacement curves for the clamped semi-cylindrical shell with the distorted mesh patterns shown in Fig. 18.

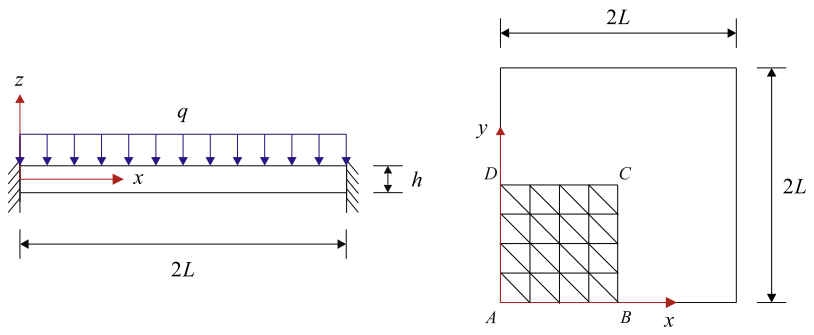

Fig. 20. Fully clamped plate under uniform pressure and mesh used (4×4).

rotations. This structure is modeled using a 6×30 element mesh of the MITC4 shell element and the corresponding MITC3 and MITC3+ shell element meshes, see Fig. 9(b). The reference solutions are obtained using a 12×60 element mesh of the MITC9 shell element.

The load–displacement curves at two different points, A and B, are depicted in Fig. 10. The deformed configurations calculated using the MITC4, MITC3 and MITC3+ shell elements are shown in Fig. 11. As seen, the MITC3 shell element displays too stiff a behavior. However, the results using the MITC3+ shell element are in agreement with those using the MITC4 shell element and reasonably close to the reference solutions.

4.4. Hemispherical shell subjected to alternating radial forces

Here we consider a hemispherical shell with an 18° circular cutout, as shown in Fig. 12(a). The shell is pinched along one direction at points B and D and pulled along the perpendicular direction at points A and C [13,15,23,24,26]. The material and geometric properties are given by $E = 6.825 \times 10^7$, $v = 0.3$, $R = 10$, and the thickness

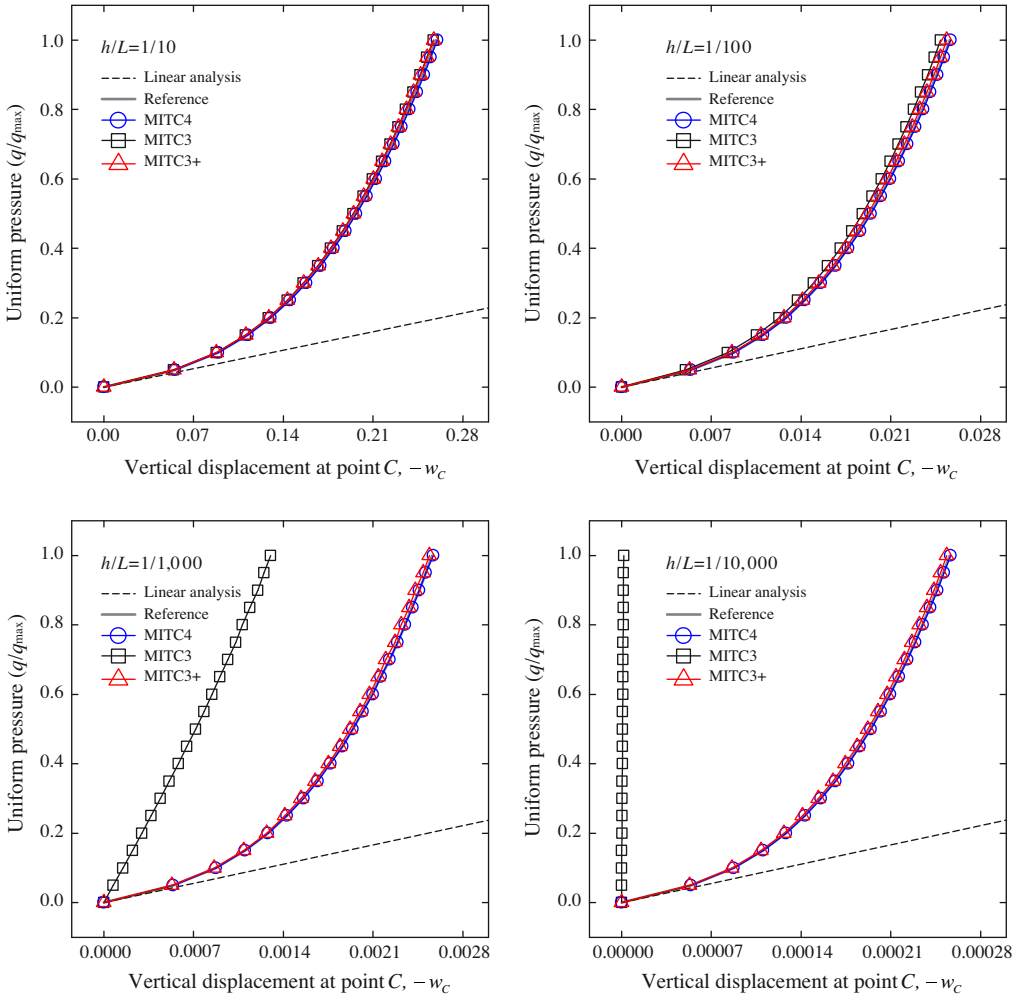

Fig. 21. Load–displacement curves for the fully clamped plate under uniform pressure.

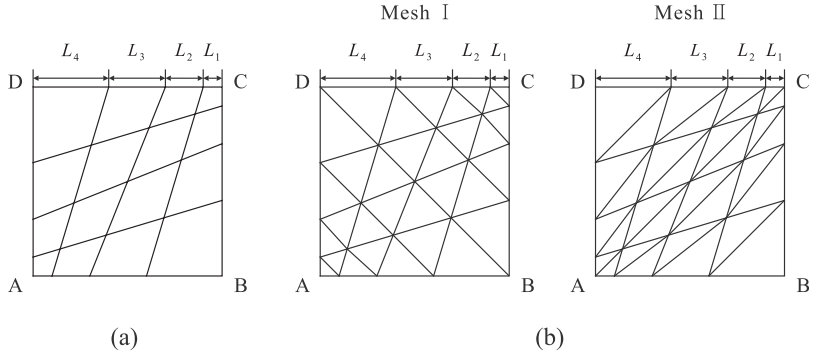

Fig. 22. Distorted meshes of the fully clamped plate (a) for the MITC4 shell element and (b) for the MITC3 and MITC3+ shell elements.

is 0.04. The point load is incrementally applied to a maximum value $P_{max} = 400$. The shell is modeled using 8×32 and 12×48 element meshes of the MITC4 shell element and the corresponding MITC3 and MITC3+ shell element meshes, see Fig. 12(b). A 24×96 element mesh of the MITC9 shell element is used to obtain the reference solutions.

Fig. 13 shows the load-radial displacement curves at the loaded points *A* and *B*. The deformed configurations obtained using a 8×32 element mesh of the MITC4 shell element and the corresponding MITC3 and MITC3+ shell element meshes are shown in Fig. 14. For the meshes used, the MITC4 and MITC3+ shell elements produce much better solution accuracy than the MITC3 shell element in this problem.

4.5. Clamped semi-cylindrical shell under point load

A well-known benchmark problem for geometric nonlinear analysis of shells is the semi-cylindrical shell under a point load shown in Fig. 15(a) [16,19,21,27]. The length and radius of the half cylinder are $L = 0.3048$ and $R = 1.016$, respectively, and the thickness is $h = 0.03$; the material constants are $E = 2.0685 \times 10^7$ and $v = 0.3$. The load applied to the shell increases up to $P_{max} = 2000$. The structure is modeled using 20×20 and 32×32 element meshes of the MITC4 shell element and the corresponding MITC3 and MITC3+ shell element meshes, see Fig. 15(b). The reference solutions are obtained using a 64×64 element mesh of the MITC9 shell element.

Fig. 16 gives the obtained load–displacement curves, and Fig. 17 shows the deformed shapes calculated using the 20×20 element mesh of the MITC3+ shell finite elements at various load levels, $P = P_{max}/3$, $2P_{max}/3$, and P_{max}. The three shell elements show good performance in the solution of this shell problem with the meshes used.

We then perform the analysis with the distorted mesh patterns shown in Fig. 18. For an $N \times N$ element mesh, each edge is discretized with the following ratio: $L_1 : L_2 : L_3 : \ldots L_N = 1:2:3:\ldots N$. The solutions are obtained with a 24×24 element mesh of the MITC4, MITC3 and MITC3+ shell elements. Fig. 19 shows the calculated load–displacement curves when the distorted mesh patterns in Fig. 18 are used. The MITC3+ shell element shows a good performance regardless of which mesh pattern in Fig. 18(b) is used.

4.6. Fully clamped plate under uniform pressure

Fig. 20 shows the fully clamped plate under uniform pressure [14,17,22,26,28,29]. A square plate of dimensions $2L \times 2L$ and uniform thickness *h* is considered and all edges are fully clamped with the hard boundary condition [2]. Due to symmetry, only one-quarter of the plate is modeled, with the following boundary conditions: $u_x = \theta_y = 0$ along *BC*, $u_y = \theta_x = 0$ along *DC* and $u_x = u_y = \theta_x = \theta_y = 0$ along *AB* and *AD*. The material properties used are $E = 1.7472 \times 10^3$ and $v = 0.3$. The pressure applied to the plate increases up to $q_{max} = h^3 \times 10^5$. The length of the plate is $L = 1$ and four different plate thicknesses ($h/L = 1/10, 1/100, 1/1{,}000$

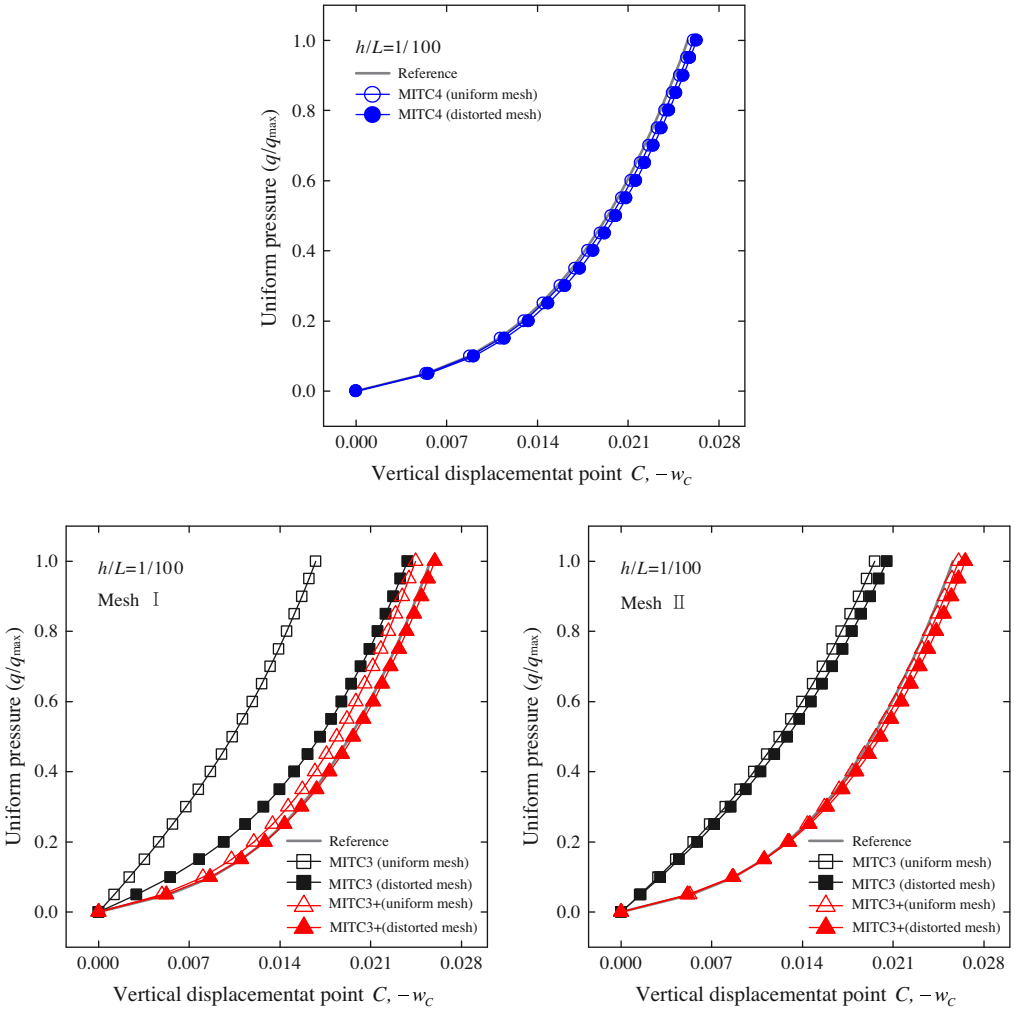

Fig. 23. Load–displacement curves for the fully clamped plate with the distorted meshes shown in Fig. 22.

and 1/10,000) are considered. This problem is modeled using a 10×10 element mesh of the MITC4 shell element and the corresponding MITC3 and MITC3+ shell element meshes. The reference solutions are calculated using a 20×20 element mesh of the MITC9 shell element.

Fig. 21 shows the calculated vertical displacement at point C versus the uniform pressure. The solutions using the MITC3 shell element deteriorate as the shell thickness decreases due to shear locking. However, the MITC3+ and MITC4 shell finite elements show excellent results compared to the reference solutions.

We also consider the same problem with the distorted 4×4 element mesh shown in Fig. 22 when $h/L = 1/100$. In the distorted element meshes, each edge is divided by the ratio: $L_1:L_2:L_3:L_4 = 1:2:3:4$. Fig. 23 shows the calculated load–displacement curves. The MITC3+ and MITC4 shell elements show an excellent performance even when the distorted meshes are used. It is also observed that, compared to the MITC3 shell element, the MITC3+ shell element gives less sensitive solutions to mesh patterns.

5. Conclusions

In this paper, the formulation of the MITC3+ shell element was extended to geometric nonlinear analysis. The total Lagrangian formulation is employed allowing for large displacements and large rotations. The nonlinear formulation is based on the same discretization assumptions that are employed in the linear formulation of the element. The nonlinear performance of the MITC3+ shell element was numerically investigated by solving several benchmark problems. In the tests considered, the predictive capability of the MITC3+ shell element is seen to be much better than of the MITC3 shell element. Indeed, the MITC3+ element gave practically as accurate results as the MITC4 shell element.

Considering also the excellent behavior of the MITC3+ shell element in linear analysis [1], we can conclude that the element is a very attractive element for general shell analyses. In future studies, it would be valuable to further develop the formulation for large strain solutions of shell structures [30], and to possibly enrich the displacement fields by using interpolation covers [31].

Acknowledgements

This work was supported by the Basic Science Research Program through the National Research Foundation of Korea (NRF) funded by the Ministry of Education, Science and Technology (No. 2014R1A1A1A05007219), and the Human Resources Development (No. 20134030200300) of the Korea Institute of Energy Technology Evaluation and Planning (KETEP) grant funded by the Korea government Ministry of Trade, Industry and Energy.

References

[1] Lee Y, Lee PS, Bathe KJ. The MITC3+ shell element and its performance. Comput Struct 2014;138:12–23.
[2] Bathe KJ. Finite element procedures. 2nd ed, 2014. Watertown, MA.
[3] Lee PS, Bathe KJ. On the asymptotic behavior of shell structures and the evaluation in finite element solutions. Comput Struct 2002;80:235–55.
[4] Chapelle D, Bathe KJ. The finite element analysis of shells – fundamentals. 2nd ed. Berlin: Springer-Verlag; 2011.
[5] Bathe KJ, Lee PS. Measuring the convergence behavior of shell analysis schemes. Comput Struct 2011;89:285–301.
[6] Lee PS, Bathe KJ. Development of MITC isotropic triangular shell finite elements. Comput Struct 2004;82:945–62.
[7] Lee Y, Yoon K, Lee PS. Improving the MITC3 shell finite element by using the Hellinger–Reissner principle. Comput Struct 2012;110–1:93–106.
[8] Chapelle D, Bathe KJ. The mathematical shell model underlying general shell elements. Int J Num Methods Eng 2000;48:289–313.
[9] Lee PS, Bathe KJ. Insight into finite element shell discretizations by use of the "basic shell mathematical model". Comput Struct 2005;83:69–90.
[10] Argyris J. An excursion into large rotations. Comput Methods Appl Mech Eng 1982;32:85–155.
[11] Bathe KJ, Lee PS, Hiller JF. Towards improving the MITC9 shell element. Comput Struct 2003;81:477–89.
[12] Lee PS, Bathe KJ. The quadratic MITC plate and MITC shell elements in plate bending. Adv Eng Software 2010;41:712–28.
[13] Jiang L, Chernuka MW. A simple four-noded corotational shell element for arbitrarily large rotations. Comput Struct 1994;53:1123–32.
[14] To CWS, Liu ML. Hybrid strain based three node flat triangular shell elements – II. Numerical investigation of nonlinear problems. Comput Struct 1995;54:1057–76.
[15] Briassoulis D. Non-linear behaviour of the RFNS element – large displacements and rotations. Comput Method Appl Mech Eng 2003;192:2909–24.
[16] Sze KY, Liu XH, Lo SH. Popular benchmark problems for geometric nonlinear analysis of shell. Finite Elem Anal Des 2004;40:1551–69.
[17] Hsiao KM, Chen YR. Nonlinear analysis of shell structures by degenerated isoparametric shell element. Comput Struct 1989;31:427–38.
[18] Simo JC, Fox DD, Rifai MS. On a stress resultant geometrically exact shell model. Part III: computational aspects of the nonlinear theory. Comput Method Appl Mech Eng 1990;70:21–70.
[19] Arciniega RA, Reddy JN. Tensor-based finite element formulation for geometrically nonlinear analysis of shell structures. Comput Method Appl Mech Eng 2007;196:1048–73.
[20] Başar Y, Ding Y. Finite-rotation shell elements for the analysis of finite-rotation shell problems. Int J Num Methods Eng 1992;34:165–9.
[21] Brank B, Perić D, Damjanić FB. On implementation of a nonlinear four node shell finite element for thin multilayered elastic shells. Comput Mech 1995;16:341–59.
[22] Kim CH, Sze KY, Kim YH. Curved quadratic triangular degenerated- and solid-shell elements for geometric non-linear analysis. Int J Num Methods Eng 2003;57:2077–97.
[23] Sansour C, Bocko J. On hybrid stress, hybrid strain and enhanced strain finite element formulations for a geometrically exact shell theory with drilling degrees of freedom. Int J Num Methods Eng 1998;43:175–92.
[24] Sansour C, Kollmann FG. Families of 4-node and 9-node finite elements for a finite deformation shell theory. an assessment of hybrid stress, hybrid strain and enhanced strain elements. Comput Mech 2000;24:435–47.
[25] Hong WI, Kim JH, Kim YH, Lee SW. An assumed strain triangular curved solid shell element formulation for analysis for plates and shells undergoing finite rotations. Int J Num Methods Eng 2001;52:747–61.
[26] Providas E, Kattis MA. A simple finite element model for the geometrically nonlinear analysis of thin shells. Comput Mech 1999;24:127–37.
[27] Klinkel S, Gruttmann W, Wagner W. A continuum based three-dimensional shell element for laminated structures. Comput Struct 1999;71:43–62.
[28] Bucalem ML, Nóbrega SHS. A mixed formulation for general triangular isoparametric shell elements based on the degenerated solid approach. Comput Struct 2000;78:35–44.
[29] Kim JH, Kim YH. A three-node C^0 ANS element for geometrically non-linear structural analysis. Comput Method Appl Mech Eng 2002;191:4035–59.
[30] Sussman T, Bathe KJ. 3D-shell elements for structures in large strains. Comput Struct 2013;122:2–12.
[31] Jeon HM, Lee PS, Bathe KJ. The MITC3 shell finite element enriched by interpolation covers. Comput Struct 2014;134:128–42.